

# Lawrence Berkeley National Laboratory

## Recent Work

**Title**

Stable Dopant-Free Asymmetric Heterocontact Silicon Solar Cells with Efficiencies above 20%

**Permalink**

<https://escholarship.org/uc/item/3km103c8>

**Journal**

ACS Energy Letters, 3(3)

**ISSN**

2380-8195

**Authors**

Bullock, J  
Wan, Y  
Xu, Z  
et al.

**Publication Date**

2018-03-09

**DOI**

10.1021/acsenergylett.7b01279

Peer reviewed

# **Stable Dopant-Free Asymmetric Heterocontact Silicon Solar Cells with Efficiencies Above 20%**

James Bullock<sup>1,2,‡</sup>, Yimao Wan<sup>1,2,3,‡</sup>, Zhaoran Xu<sup>1,2</sup>, Stephanie Essig<sup>4</sup>, Mark Hettick<sup>1,2</sup>, Hanchen Wang<sup>1,2</sup>, Wenbo Ji<sup>1,2</sup>, Mathieu Boccard<sup>4</sup>, Andres Cuevas<sup>3</sup>, Christophe Ballif<sup>4</sup> and Ali Javey<sup>1,2,\*</sup>

<sup>1</sup>*Department of Electrical Engineering and Computer Sciences, University of California, Berkeley, California 94720, USA.*

<sup>2</sup>*Materials Sciences Division, Lawrence Berkeley National Laboratory, Berkeley, California 94720, USA.*

<sup>3</sup>*Research School of Engineering, The Australian National University (ANU), Canberra, ACT 0200, Australia*

<sup>4</sup>*École Polytechnique Fédérale de Lausanne (EPFL), Institute of Micro Engineering (IMT), Photovoltaics and Thin Film Electronic Laboratory (PVLab), Maladière 71b, CH-200 Neuchatel, Switzerland*

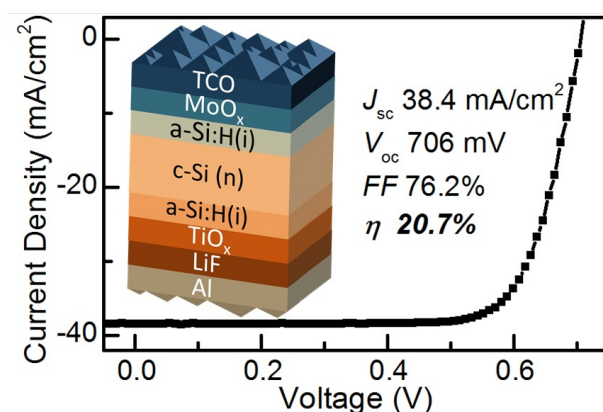
<sup>‡</sup> *These authors have contributed equally to this work*

<sup>\*</sup> *corresponding author: Ali Javey (ajavey@berkeley.edu)*

## Abstract

Development of new device architectures and process technologies are of tremendous interest in crystalline silicon (c-Si) photovoltaics to drive enhanced performance and/or reduced processing cost. In this regard, an emerging concept with a high efficiency potential is to employ low/high work function metal compounds or organic materials to form asymmetric electron and hole heterocontacts. This paper demonstrates two important milestones in advancing this burgeoning concept. Firstly, a high-performance, low-temperature, electron-selective heterocontact is developed, comprised of a surface passivating a-Si:H layer, a protective  $\text{TiO}_x$  interlayer and a low work function  $\text{LiF}_x/\text{Al}$  outer electrode. This is combined with a  $\text{MoO}_x$  hole-selective heterocontact to demonstrate a cell efficiency of 20.7% - the highest value for this cell class to date. Secondly, we show that this cell passes a standard stability test by maintaining >95% of its original performance after 1000 hours of unencapsulated damp-heat exposure, indicating its potential for longevity.

TOC Figure



In recent times, there has been a significant increase in the use of metal oxides,<sup>1-6</sup> fluorides,<sup>7-9</sup> sulphides,<sup>10</sup> and organic materials<sup>11,12</sup> as carrier selective heterocontacts for crystalline silicon (c-Si) photovoltaic (PV) devices. This research stream has been motivated by potential advantages associated with fabrication simplicity and cost reduction. Such materials can be deposited at low temperature (< 200°C) using simple techniques, to form full-area heterocontacts with optical characteristics tailored for either the sunward- or rear-side of a solar cell. These heterocontacts can also overcome or reduce losses common to other c-Si cell architectures—for example, parasitic absorption or heavy impurity doping losses<sup>7,13-15</sup>—increasing the practical efficiency limit of this structure. Most efforts so far have focused on substituting one such heterocontact into an otherwise conventional c-Si cell,<sup>16-20</sup> demonstrating, in many cases, clear performance or fabrication advantages. The ultimate extension of this concept is to use a set of asymmetric heterocontacts in a single cell structure, sometimes referred to as the dopant-free asymmetric heterocontact or DASH cell. In our previous study, we presented a record 19.4% efficient DASH solar cell,<sup>7</sup> utilizing MoO<sub>x</sub> and LiF<sub>x</sub> based heterocontacts with thin amorphous silicon (a-Si:H) interfacial passivation layers. Although promising for a first proof-of-concept, it is important to demonstrate that higher conversion efficiencies can be achieved, in line with the suggested higher efficiency potential of this architecture. Further, for a new technology to be considered in a field such as c-Si PV, it must satisfy additional requirements related to thermal steps

during cell and module fabrication and to device longevity in operation. Therefore, in this study the DASH cell structure is revisited with a particular emphasis on simultaneously improving the device efficiency and stability. Modifications to the structure and fabrication allow us to show for the first time that this technology is compatible with efficiencies greater than 20%. We also show that un-encapsulated DASH devices can pass an accelerated environmental test designed to simulate the expected damp-heat stressors presented to a solar cell over its lifetime.

To increase the DASH cell performance, improvements must be made simultaneously to both the electron and hole heterocontacts. A recent study conducted by co-authors has shown the thermal stability of the hole heterocontact can be improved via an additional annealing step prior to the  $\text{MoO}_x$  deposition.<sup>21</sup> In this study, we focus on the electron side, aiming to develop a thermally robust rear heterocontact. The electron-selective heterocontact of our first-generation DASH cell utilized a low work function ( $\sim 1 \text{ nm}$ )  $\text{LiF}_x / \text{Al}$  outer stack to efficiently extract electrons. When applied to c-Si the low work function induces downward band-bending, encouraging electrons to the surface. To improve the stability of this contact, here we integrate thin oxide protective layers to prevent interaction between the thin  $a\text{-Si:H}$  passivation layer and the  $\text{LiF}_x / \text{Al}$  layers, without causing a significant impediment to electron flow. Four candidate oxides are trialled in this application: Titanium oxide ( $\text{TiO}_x$ ), Tantalum oxide ( $\text{Ta}_2\text{O}_x$ ), Hafnium oxide ( $\text{HfO}_x$ ) and Aluminium oxide ( $\text{Al}_2\text{O}_x$ ). All are deposited via atomic layer

deposition (ALD) at temperatures  $\leq 150^{\circ}\text{C}$  (further details can be found in Table 1). These materials are chosen to study the influence of conduction band offset on the electron contact performance. To firstly quantify the conduction band offset, Figure 1 presents the measured optoelectronic properties of  $\text{TiO}_x$ ,  $\text{Ta}_2\text{O}_x$ ,  $\text{HfO}_x$  and  $\text{Al}_2\text{O}_x$  thin films ( $\sim 15 \text{ nm}$ ) deposited on polished c-Si wafers. The work function and valence band spectrum, measured by X-ray Photoelectron Spectroscopy (XPS), are presented in Figure 1a and b, respectively. The oxygen and metal core levels are also measured by XPS, revealing the stoichiometry of  $\text{TiO}_x$  ( $x = 2.02$ ),  $\text{Ta}_2\text{O}_x$  ( $x = 5.0$ ),  $\text{HfO}_x$  ( $x = 1.93$ ) and  $\text{Al}_2\text{O}_x$  ( $x = 2.98$ ). This is accompanied by the refractive indices ( $n, k$ ) presented in Figure 1c, extracted from spectroscopic ellipsometry. Implicit within this modelling is a fitting of the optical bandgap  $E_g$ , which is included for each oxide in the bottom plot. Combining the extracted  $E_g$  with the XPS results in Figure 1a and b allows an estimation of the band positions of these oxides relative to c-Si. As shown in Figure 1d an increasing conduction band offset can be expected for the four materials,  $\text{TiO}_x < \text{Ta}_2\text{O}_x < \text{HfO}_x < \text{Al}_2\text{O}_x$ . The  $\text{Ta}_2\text{O}_x$  and  $\text{TiO}_x$  films show the lowest conduction band offsets and hence they should present the smallest impediment to electron flow.

To test this electrically,  $\text{TiO}_x$ ,  $\text{Ta}_2\text{O}_x$ ,  $\text{HfO}_x$  and  $\text{Al}_2\text{O}_x$  films of  $\sim 3 \text{ nm}$  are inserted on the rear side of  $2 \times 2 \text{ cm}^2$  solar cells with the structure shown in Figure 2a. These cells, referred to here as hybrid cells, utilize a standard silicon heterojunction (SHJ) sunward-side hole contact for simplicity,<sup>22</sup> further

details of which can be found in the Methods section. Contrary to our previous studies, a sub-nanometer layer of  $\text{LiF}_x$  ( $\sim 0.6$  nm) is used between the metal oxide and Al layers, as it was found to provide the lowest resistivities for this heterocontact stack. The photovoltaic current density-voltage  $JV$  behaviour, measured under standard 1-sun conditions (25°C, 100 mW/cm<sup>2</sup> AM 1.5G spectrum), is shown in Figure 2b. A clear trend of decreasing fill factor  $FF$ , due to increasing series resistance  $R_s$ , is observed, in line with the increasing conduction band offset discussed above. Series resistance values extracted from these  $JV$  curves are included in Figure 2b. The results indicate that, among these materials,  $\text{TiO}_x$  produces the lowest  $R_s$ , likely due to its small conduction band offset with c-Si and hence this material is studied in greater detail. The potential of  $\text{TiO}_x$  for electron extraction / injection has been demonstrated on a number of optoelectronic devices, including solar cells made from a range of absorber materials.<sup>23-25</sup> The use of  $\text{TiO}_x$  electron heterocontacts in c-Si solar cells has expanded rapidly in recent years, being trialled directly,<sup>12,26</sup> with passivating layers,<sup>18,27</sup> and with low work function metals.<sup>16,28</sup> The heterocontact explored here is unique in the combination of passivation, protection and low work function from the  $a\text{-Si:H}$ ,  $\text{TiO}_x$  and  $\text{LiF}_x$  / Al layers. This provides a stable, full-area contact deposited via simple means with high rear reflection. Figure 2c shows  $JV$  curves measured on hybrid cells with different  $\text{TiO}_x$  thicknesses ranging from 6 nm to 1.5 nm. The three solid lines correspond to the  $JV$  curves of cells cut from the same wafer and processed in parallel, showing

that the thinnest film of 1.5 nm exhibits the smallest series resistance. Thinner films were not trialled due to the likelihood of incomplete surface coverage, and cells made without any  $\text{TiO}_x$  (not shown) had lower open circuit voltage  $V_{oc}$  and  $FF$  values than those with the 1.5 nm  $\text{TiO}_x$  film. The dotted line represents the best of five devices measured on a full (uncut) wafer processed using the same  $a\text{-Si:H} / \text{TiO}_x$  (1.5 nm) /  $\text{LiF}_x$  ( $\sim$ 0.6 nm) / Al rear electron contact. This hybrid cell reaches an efficiency of 20.9%, supported by a  $V_{oc}$  of 713 mV and a  $FF$  of 78.1%.

As discussed above, the primary role of the  $\text{TiO}_x$  interlayer is to improve the stability of the device. To investigate this effect, a set of four transfer-length-method (TLM) samples was prepared on n-type  $c\text{-Si}$  (1  $\Omega\text{cm}$ ) for the extraction of contact resistivity  $\rho_c$ . These four test samples, were fabricated with the following contact stacks: *i.*  $a\text{-Si:H} / \text{TiO}_x$  (1.5 nm) /  $\text{LiF}_x$  ( $\sim$ 0.6 nm) / Al; *ii.*  $a\text{-Si:H} / \text{LiF}_x$  ( $\sim$ 0.6 nm) / Al; *iii.*  $\text{TiO}_x$  (1.5 nm) /  $\text{LiF}_x$  ( $\sim$ 0.6 nm) / Al; and *iv.*  $\text{LiF}_x$  ( $\sim$ 0.6 nm) / Al. Figure 3a shows the measured  $\rho_c$  of the four samples as a function of annealing temperature in air. The measurements were taken after successive 10 minute anneals at incrementally increasing temperatures between room temperature and 300°C; hence the last point corresponds to a cumulative annealing time of 50 min. It can be seen that the addition of the 1.5 nm  $\text{TiO}_x$  layer does not increase the as-deposited  $\rho_c$ . This is true for both contacts with and without the  $a\text{-Si:H}$  layers with  $\rho_c$  values of  $\sim$ 70  $\text{m}\Omega\text{cm}^2$  and 4  $\text{m}\Omega\text{cm}^2$ , respectively. More importantly, the  $\text{TiO}_x$  layer improves the thermal stability of  $\rho_c$  drastically for annealing temperatures up

to 300°C. It should be noted that TLM samples fabricated without the LiF<sub>x</sub> interlayer (not shown) exhibited significantly higher  $\rho_c$  values than those shown in Figure 3a.

A second stability test, conducted on two hybrid solar cells with and without a 1.5 nm TiO<sub>x</sub> layer, is presented in Figure 3b. Whereas the  $V_{oc}$  of the cell without TiO<sub>x</sub> degrades drastically as the annealing temperature increases, a significant improvement in the passivation stability is achieved as a result of the TiO<sub>x</sub> interlayer addition. The enhanced stability results presented in Figure 3a for the  $\rho_c$  and in Figure 3b for the  $V_{oc}$  are likely due to the prevention of intermixing between the a-Si:H and the LiF<sub>x</sub> / Al layers. TiO<sub>x</sub> protective layers have been utilized in a number of silicon based structures, including photoelectrochemical cells as a protective film in harsh chemical environments,<sup>29</sup> and in microelectronics and solar cell devices as a high temperature diffusion barrier to metals and dopants.<sup>30,31</sup> Without this layer, at elevated temperatures the angstrom-scale LiF<sub>x</sub> (~0.6 nm) may not provide sufficient protection of the thin a-Si:H passivation layer from the overlying Al layer. A number of studies have shown metal-induced crystallization of a-Si:H at low temperatures upon contact with Al,<sup>32-34</sup> a process which will increase interface recombination.

Finally, the optimized a-Si:H / TiO<sub>x</sub> / LiF<sub>x</sub> / Al electron heterocontact is combined with a front, a-Si:H / MoO<sub>x</sub> / indium tin oxide (ITO) hole heterocontact into a full 2×2 cm<sup>2</sup> DASH cell with the structure shown in Figure 4a. The front MoO<sub>x</sub> heterocontact fabrication is conducted in line with

the suggestions of Ref 21 to improve its thermal stability. The 1-sun  $J/V$  results of the stability enhanced DASH is provided in Figure 4b, showing that a conversion efficiency of 20.7% has been achieved, supported by a  $V_{oc}$  of 706 mV and a  $FF$  of 76.1%. This is the first demonstration of a DASH cell above 20%. A quantum efficiency analysis of this cell is also included in Figure 4c, showing the measured external quantum efficiency (EQE), reflection and internal quantum efficiency (IQE), taken in-between Ag metal grid fingers. After accounting for a contact fraction of  $\sim 3\%$ , the integration of the EQE and the solar spectrum product gives a  $J_{sc}$  of 38.8 mA/cm<sup>2</sup>. This value agrees well with that obtained directly from the light  $J/V$  of 38.4 mA/cm<sup>2</sup> supporting the accuracy of the value. To further test the stability of the electron and hole contact structures, a representative un-encapsulated DASH cell is subjected to a standard 1000-hour damp-heat test at 85°C and 85% relative humidity(RH). Table 1 shows the measured characteristic parameters of this device before and after the 1000-hour period, revealing that 96% of the original performance has been maintained.

In this article we have simultaneously improved the benchmark efficiency and stability of c-Si DASH solar cells. We have found that the thermal stability of the electron-selective heterocontacts can be improved by introducing a protective TiO<sub>x</sub> interlayer between the a-Si:H passivation layer and the low work function LiF<sub>x</sub> / Al electrode. This second-generation DASH cell has been proven to maintain  $> 95\%$  of its performance after 1000 hours of unencapsulated damp-heat exposure. Importantly, the improved stability

does not come at the expense of performance. On the contrary, a conversion efficiency of 20.7% has been demonstrated, the highest value of any DASH solar cell presented to date. These developments in efficiency and stability pave the way for the DASH cell design to become a viable contender for high performance, low-cost c-Si PV.

### **Materials characterization:**

Samples for X-ray Photoelectron Spectroscopy (XPS) and Spectroscopic Ellipsometry (SE) were fabricated by depositing thin films of  $\text{TiO}_x$ ,  $\text{Ta}_2\text{O}_x$ ,  $\text{HfO}_x$  and  $\text{Al}_2\text{O}_x$  on a polished n<sup>+</sup> silicon wafer which was given a short 5% HF etch prior to deposition. The thin films were deposited by atomic-layer-deposition (ALD), with a chamber temperature of  $\leq 150^\circ\text{C}$ . Further details can be found in Table 1. XPS measurements were performed in a Kratos spectrometer with an Al monochromatic X-ray source. All measurements were performed on thin films ( $\sim 15$  nm) without electron gun neutralization. Charging is known to be a general issue in XPS, particularly for insulating films. Efforts were made to minimize charging by reducing incident X-ray exposure during the secondary electron cutoff measurement, and core level and valence band spectra were referenced to a C 1s peak at 284.8eV. For the secondary electron cutoff measurement, a sputter cleaned Au sample was included in each run as a reference. The ranges provided for the Fermi energy, conduction band and valence band of each material in the schematic of

Figure 1d are based off the measured variation in XPS results. SE measurements were also taken on ~15nm films with a JA Wollam M 2000 spectroscopic ellipsometer and the films were fitted with Tauc-Lorentz models, the optical bandgaps of which are listed in Table 1.

### **Device fabrication and characterization.**

Contact structures were fabricated according to a transfer-length-method (TLM) design. Samples with and without the thin (~5nm) a-Si:H passivation layer were deposited on 4 Ωcm and 1 Ωcm n-type float zone (FZ) wafers, respectively. The a-Si:H was deposited via plasma enhanced chemical vapor deposition (PECVD). Half of these received a thin 1.5 nm TiO<sub>x</sub> protective layer following which they were all deposited with a LiF<sub>x</sub> (0.6 nm) / Al electrode, through a shadow mask to achieve the TLM pattern. The dark current-voltage *I/V* behaviour was measured as a function of pad spacing using a Keithley 2400 sourcemeter and the contact resistivity was extracted from this relationship according to Ref 35. Annealing of contact samples was performed on a hotplate in air at temperatures between 100°C and 300°C.

The hybrid cell structures utilized in Figures 2 and 3 were fabricated on double side textured, float zone, 4 Ωcm n-type wafers with a thickness of ~250 μm. The front hole heterocontact consists of a stack of intrinsic (~5 nm) and boron doped (~10 nm) a-Si:H layers. This is capped with an indium tin oxide (ITO) layer which was sputtered through a shadow mask to define a 2×2 cm<sup>2</sup> area. The a-Si:H layers were deposited via plasma enhanced

chemical vapor deposition (PECVD) and the TCOs via DC sputtering. The front Ag grid, with a surface fraction of ~3%, is achieved by screen printing a low temperature Ag paste and curing. For the rear contact, an intrinsic thin a-Si:H layer (~5nm) is coated with either TiO<sub>x</sub>, Ta<sub>2</sub>O<sub>x</sub>, HfO<sub>x</sub> or Al<sub>2</sub>O<sub>x</sub> thin films deposited via ALD using the precursors listed in Table 1. These are capped with a low work function LiF<sub>x</sub> (~0.6 nm) / Al (~200 nm) electrode deposited via thermal evaporation. Hybrid cell annealing was performed in a quartz tube furnace between 100°C and 300°C.

The 2×2 cm<sup>2</sup> DASH cell was also fabricated on a double side textured 4 Ωcm n-type wafer with a thin (~5 nm) passivating a-Si:H layer on either side. This was subjected to a short anneal at 250°C prior to contact deposition in line with the suggestions of Ref 21. Next, the front-side was deposited with ~5 nm of thermally evaporated MoO<sub>x</sub> followed by ~70 nm of sputtered indium tin oxide (ITO) and finally low temperature Ag paste was screen printed and cured at 190°C. The rear side was deposited with 1.5 nm of ALD TiO<sub>x</sub> followed by the thermally evaporated LiF<sub>x</sub> (~0.6 nm) / Al electrode.

One sun *JV* analysis of these cells was performed under standard conditions (25°C, 100 mW/cm<sup>2</sup>, AM 1.5G spectrum) using a calibrated solar simulator and an aperture mask to avoid peripheral absorption. The external quantum efficiency and reflection were measured in an in-house built setup. An Espec LHU humidity chamber, held at 85°C and 85% RH, was used for the humidity exposure test.



## AUTHOR INFORMATION

### **Corresponding Author**

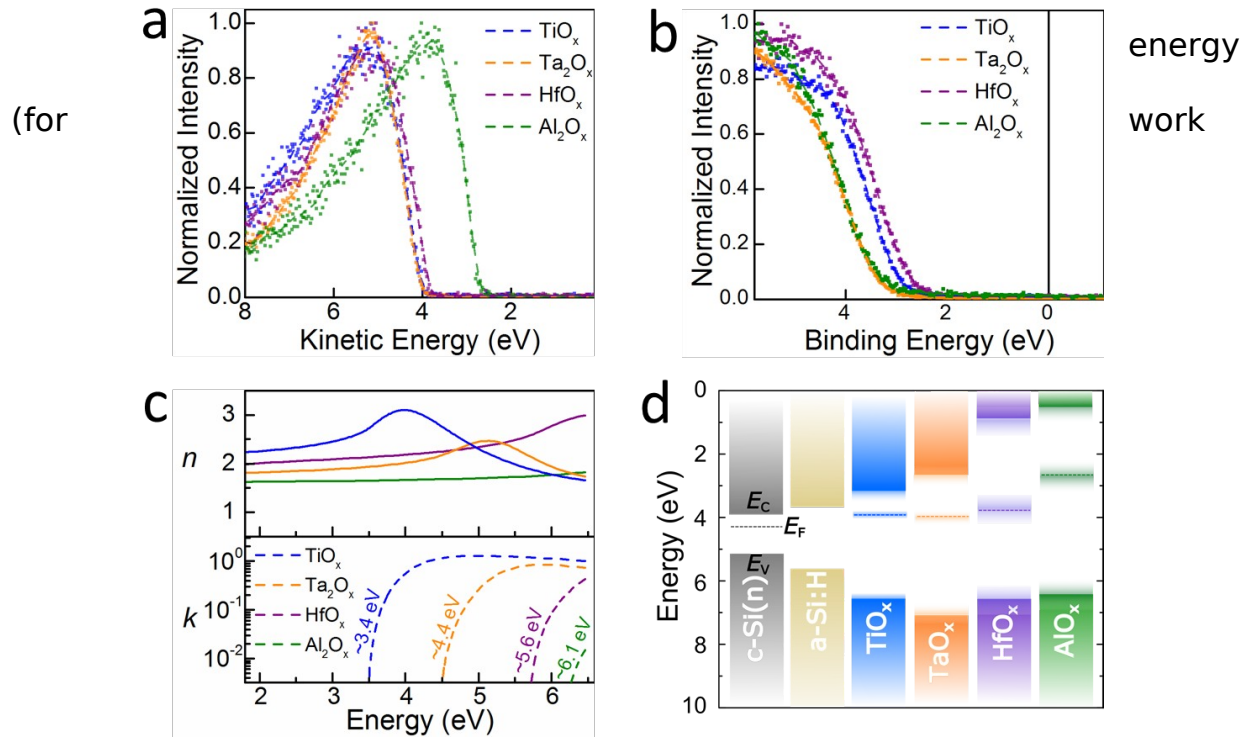
\*E-mail: [ajavey@berkeley.edu](mailto:ajavey@berkeley.edu)

### **Acknowledgements**

Device design, fabrication and characterization at Berkeley were funded by the U.S. Department of Energy, Solar Energy Technologies Office. Materials characterization was supported by the Electronic Materials Programs, funded by the Director, Office of Science, Office of Basic Energy Sciences, Material Sciences and Engineering Division of the US Department of Energy under Contract No. DE-AC02-05CH11231. XPS characterization was performed at the Joint Center for Artificial Photosynthesis, supported through the Office of Science of the US Department of Energy under Award Number DE-SC0004993. Work at the Molecular Foundry was supported by the Office of Science, Office of Basic Energy Sciences, of the US Department of Energy (Contract No. DE-AC02-05CH11231). S. Essig held a Marie Skłodowska-Curie Individual Fellowship from the European Research Council (ERC) under the European Union's Horizon 2020 research and innovation programme (grant agreement No: 706744, action acronym: COLIBRI). Work at EPFL was financially supported by the Swiss National Science Foundation via the NRP70 "Energy Turnaround" project "PV2050". Work at the ANU was

supported by the Australian Government through the Australian Research Council (Discovery Project: DP150104331) and the Australia-US Institute for Advanced Photovoltaics (AUSIAPV) program under grant number ACAP6.9.

**Figure 1 | Electron contact materials.** **a**, Secondary electron cutoff



function), **b**, valence band spectrum, and **c**, refractive indices (top: real part  $n$ , bottom: imaginary part  $k$ ) of different metal oxide protective films. **d**, potential band position diagram for the electron heterocontact materials using information from a-c.

**Table**

Material	Metal precursor	Oxidizing precursor	Extracted $E_g$ (eV)	Oxygen : metal ratio
TiO <sub>x</sub>	Titanium isopropoxide	Water	3.45	2.02
Ta <sub>2</sub> O <sub>x</sub>	Tantalum ethoxide	Water	4.4	2.5
HfO <sub>x</sub>	Tetrakis(diethylamido)hafnium	Water	5.65	1.93
Al <sub>2</sub> O <sub>x</sub>	Trimethylaluminum	Water	6.08	1.49

**1**

|

Deposition conditions and properties of atomic-layer-deposited metal oxide protective layers.

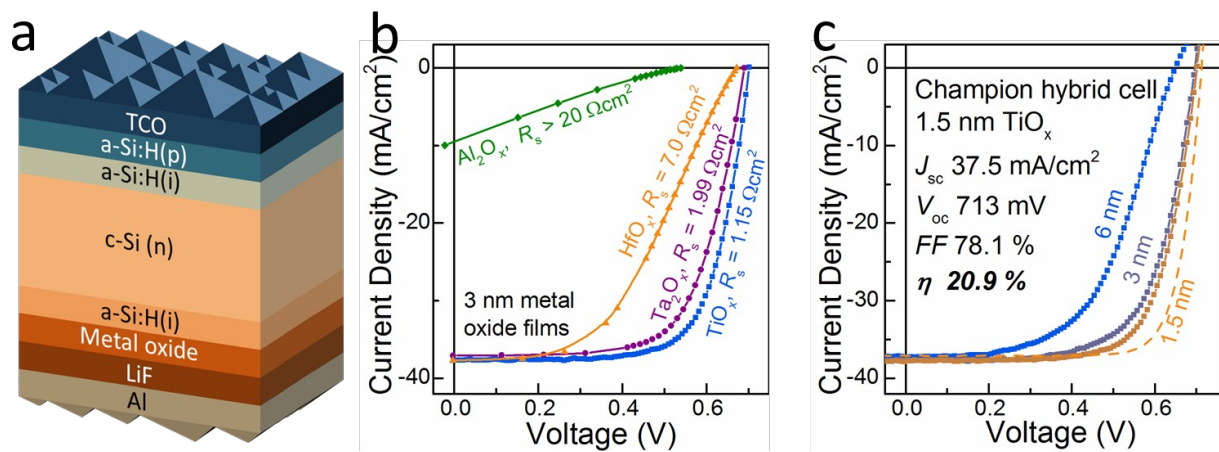
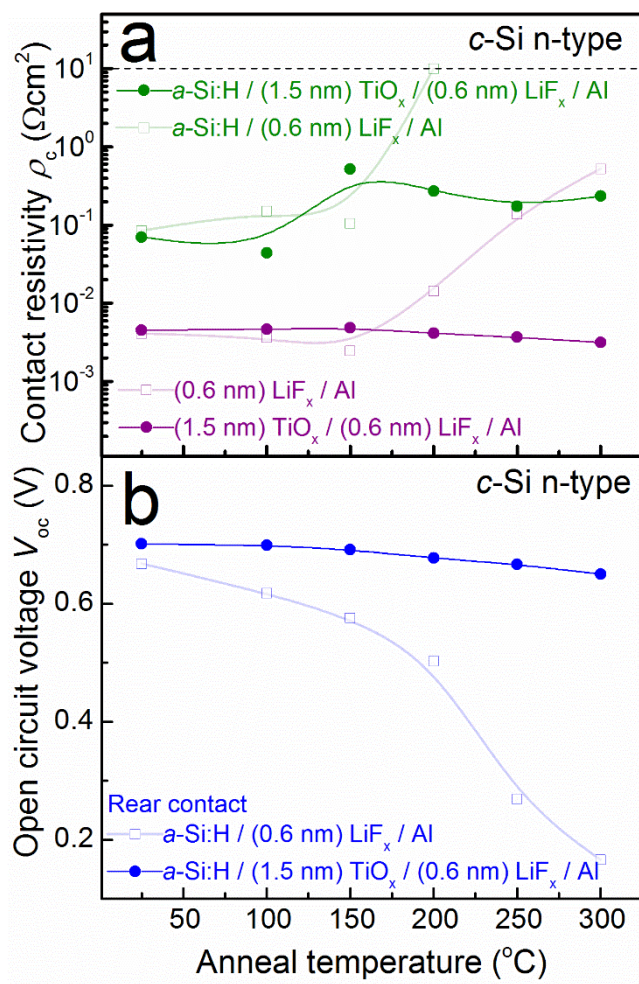


**Figure 2 | Electron contact optimization.** **a**, structure of hybrid cell used for contact optimization, **b**, 1-sun light  $J/V$  behaviour of hybrid cells with 3 nm protective metal oxide layers, **c**, 1-sun light  $J/V$  behaviour of hybrid cells with different  $\text{TiO}_x$  thicknesses showing an optimum thickness of 1.5 nm.

**Figure 3 | stability.** **a**, sequential increasing samples and  $\text{TiO}_x$  progression sequential increasing cells layer.



**Electron contact**  
 $\rho_c$  as a function of 10 minute anneals at temperatures for with/without a-Si:H layers. **b**,  $V_{\text{oc}}$  of hybrid cells after 10 minute anneals at temperatures for with/without the  $\text{TiO}_x$

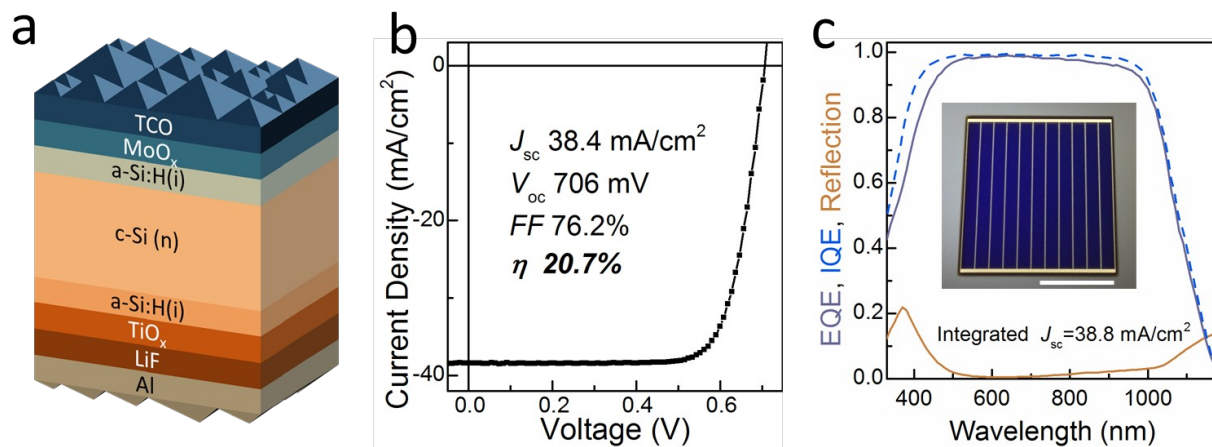


**Figure 4 | DASH cell record.** **a**, structure of the DASH cell, **b**, 1-sun light  $J/V$  behaviour of champion DASH cell, **c**, external quantum efficiency (EQE), internal quantum efficiency (IQE) and reflection of champion DASH cell, the inset shows a photograph of the cell design and the integrated  $J_{sc}$  value. The white scale bar is  $\sim 1$  cm.

<b>Table</b>		$V_{oc}$ (V)	FF (%)	$J_{sc}$ (mA/cm <sup>2</sup> )	$\eta$ (%)	<b>2</b>		<b>Damp</b>
<b>heat</b>	As fabricated	698	73.5	38.2	19.6			
	1000 hrs at 85°C, 85% RH	696	71.3	38.2	19.0			

sun JV

**2 | Damp**

**stability.** 1-

characteristics

of a representative DASH cell measured before and after 1000 hours of unencapsulated exposure to 85°C, 85% RH.

## References

- (1) Battaglia, C.; Yin, X.; Zheng, M.; Sharp, I. D.; Chen, T.; McDonnell, S.; Azcatl, A.; Carraro, C.; Ma, B.; Maboudian, R.; et al. Hole Selective MoO<sub>x</sub> Contact for Silicon Solar Cells. *Nano Lett.* **2014**, *14*, 967–971.
- (2) Avasthi, S.; McClain, W. E.; Man, G.; Kahn, A.; Schwartz, J.; Sturm, J. C. Hole-Blocking Titanium-Oxide/Silicon Heterojunction and Its Application to Photovoltaics. *Appl. Phys. Lett.* **2013**, *102*, 203901.
- (3) Wan, Y.; Samundsett, C.; Bullock, J.; Hettick, M.; Allen, T.; Yan, D.; Peng, J.; Wu, Y.; Cui, J.; Javey, A.; et al. Conductive and Stable Magnesium Oxide Electron-Selective Contacts for Efficient Silicon Solar Cells. *Adv. Energy Mater.* **2016**, *7*, 1601863.
- (4) Bivour, M.; Temmler, J.; Steinkemper, H.; Hermle, M. Molybdenum and Tungsten Oxide: High Work Function Wide Band Gap Contact Materials for Hole Selective Contacts of Silicon Solar Cells. *Sol. Energy Mater. Sol. Cells* **2015**, *142*, 34–41.
- (5) Gerling, L. G.; Mahato, S.; Morales-Vilches, A.; Masmitja, G.; Ortega, P.; Voz, C.; Alcubilla, R.; Puigdollers, J. Transition Metal Oxides as Hole-Selective Contacts in Silicon Heterojunctions Solar Cells. *Sol. Energy Mater. Sol. Cells* **2016**, *145*, 109–115.
- (6) Macco, B.; Vos, M. F. J.; Thissen, N. F. W.; Bol, A. A.; Kessels, W. M. M. Low-Temperature Atomic Layer Deposition of MoO<sub>x</sub> for Silicon Heterojunction Solar Cells. *Phys. Status Solidi RRL – Rapid Res. Lett.* **2015**, *9*, 393–396.
- (7) Bullock, J.; Hettick, M.; Geissbühler, J.; Ong, A. J.; Allen, T.; Sutter-Fella, C. M.; Chen, T.; Ota, H.; Schaler, E. W.; De Wolf, S.; et al. Efficient Silicon Solar Cells with Dopant-Free Asymmetric Heterocontacts. *Nat. Energy* **2016**, *1*, 15031.
- (8) Wan, Y.; Samundsett, C.; Bullock, J.; Allen, T.; Hettick, M.; Yan, D.; Zheng, P.; Zhang, X.; Cui, J.; McKeon, J.; et al. Magnesium Fluoride Electron-Selective Contacts for Crystalline Silicon Solar Cells. *ACS Appl. Mater. Interfaces* **2016**, *8*, 14671–14677.
- (9) Zhang, Y.; Liu, R.; Lee, S.-T.; Sun, B. The Role of a LiF Layer on the Performance of Poly(3,4-Ethylenedioxythiophene):Poly(Styrenesulfonate)/Si Organic-Inorganic Hybrid Solar Cells. *Appl. Phys. Lett.* **2014**, *104*, 083514.
- (10) Xu, X.; Bullock, J.; Schelhas, L. T.; Stutz, E. Z.; Fonseca, J. J.; Hettick, M.; Pool, V. L.; Tai, K. F.; Toney, M. F.; Fang, X.; et al. Chemical Bath Deposition of P-Type Transparent, Highly Conducting (CuS)<sub>x</sub>:(ZnS)<sub>1-x</sub> Nanocomposite Thin Films and Fabrication of Si Heterojunction Solar Cells. *Nano Lett.* **2016**, *16*, 1925–1932.
- (11) Zielke, D.; Pazidis, A.; Werner, F.; Schmidt, J. Organic-Silicon Heterojunction Solar Cells on n-Type Silicon Wafers: The BackPEDOT Concept. *Sol. Energy Mater. Sol. Cells* **2014**, *131*, 110–116.
- (12) Nagamatsu, K. A.; Avasthi, S.; Sahasrabudhe, G.; Man, G.; Jhaveri, J.; Berg, A. H.; Schwartz, J.; Kahn, A.; Wagner, S.; Sturm, J. C. Titanium Dioxide/Silicon Hole-Blocking Selective Contact to Enable Double-Heterojunction Crystalline Silicon-Based Solar Cell. *Appl. Phys. Lett.* **2015**, *106*, 123906.
- (13) Holman, Z. C.; Descoeuilles, A.; Barraud, L.; Fernandez, F. Z.; Seif, J. P.; De Wolf, S.; Ballif, C. Current Losses at the Front of Silicon Heterojunction Solar Cells. *Photovolt. IEEE J. Of* **2012**, *2*, 7–15.

- (14) Richter, A.; Glunz, S. W.; Werner, F.; Schmidt, J.; Cuevas, A. Improved Quantitative Description of Auger Recombination in Crystalline Silicon. *Phys. Rev. B* **2012**, *86*, 165202.
- (15) Battaglia, C.; de Nicolas, S. M.; De Wolf, S.; Yin, X.; Zheng, M.; Ballif, C.; Javey, A. Silicon Heterojunction Solar Cell with Passivated Hole Selective MoO<sub>x</sub> Contact. *Appl. Phys. Lett.* **2014**, *104*, 113902.
- (16) Allen, T. G.; Bullock, J.; Jeangros, Q.; Samundsett, C.; Wan, Y.; Cui, J.; Hessler-Wyser, A.; De Wolf, S.; Javey, A.; Cuevas, A. A Low Resistance Calcium/Reduced Titania Passivated Contact for High Efficiency Crystalline Silicon Solar Cells. *Adv. Energy Mater.* **2017**, *7*, 1602606.
- (17) Bullock, J.; Zheng, P.; Jeangros, Q.; Tosun, M.; Hettick, M.; Sutter-Fella, C. M.; Wan, Y.; Allen, T.; Yan, D.; Macdonald, D.; et al. Lithium Fluoride Based Electron Contacts for High Efficiency N-Type Crystalline Silicon Solar Cells. *Adv. Energy Mater.* **2016**, *6*, 1600241.
- (18) Yang, X.; Weber, K.; Hameiri, Z.; De Wolf, S. Industrially Feasible, Dopant-Free, Carrier-Selective Contacts for High-Efficiency Silicon Solar Cells. *Prog. Photovolt. Res. Appl.* **2017**, *25*, 896–904.
- (19) Masmitjà, G.; Gerling, L. G.; Ortega, P.; Puigdollers, J.; Martín, I.; Voz, C.; Alcubilla, R. V<sub>2</sub>O<sub>x</sub>-Based Hole-Selective Contacts for c-Si Interdigitated Back-Contacted Solar Cells. *J. Mater. Chem. A* **2017**, *5*, 9182–9189.
- (20) Geissbühler, J.; Werner, J.; Martin de Nicolas, S.; Barraud, L.; Hessler-Wyser, A.; Despeisse, M.; Nicolay, S.; Tomasi, A.; Niesen, B.; De Wolf, S.; et al. 22.5% Efficient Silicon Heterojunction Solar Cell with Molybdenum Oxide Hole Collector. *Appl. Phys. Lett.* **2015**, *107*, 081601.
- (21) Essig, S.; Dréon, J.; Rucavado, E.; Mews, M.; Koida, T.; Boccard, M.; Werner, J.; Geissbuhler, J.; Löper, P.; Morales-Masis, M.; et al. Towards Annealing-Stable Molybdenum-Oxide-Based Hole-Selective Contacts for Si Photovoltaics. *Sol. Rapid Res. Lett.* **2018**, In Press.
- (22) Descoeuadres, A.; Holman, Z. C.; Barraud, L.; Morel, S.; De Wolf, S.; Ballif, C. >21%; Efficient Silicon Heterojunction Solar Cells on n- and p-Type Wafers Compared. *Photovolt. IEEE J. Of* **2013**, *3*, 83–89.
- (23) Liu, M.; Johnston, M. B.; Snaith, H. J. Efficient Planar Heterojunction Perovskite Solar Cells by Vapour Deposition. *Nature* **2013**, *501*, 395.
- (24) Hsu, W.; Sutter-Fella, C. M.; Hettick, M.; Cheng, L.; Chan, S.; Chen, Y.; Zeng, Y.; Zheng, M.; Wang, H.-P.; Chiang, C.-C.; et al. Electron-Selective TiO<sub>2</sub> Contact for Cu(In,Ga)Se<sub>2</sub> Solar Cells. *Sci. Rep.* **2015**, *5*, 16028.
- (25) Yin, X.; Battaglia, C.; Lin, Y.; Chen, K.; Hettick, M.; Zheng, M.; Chen, C.-Y.; Kiriya, D.; Javey, A. 19.2% Efficient InP Heterojunction Solar Cell with Electron-Selective TiO<sub>2</sub> Contact. *ACS Photonics* **2014**, *1*, 1245–1250.
- (26) Boccard, M.; Yang, X.; Weber, K.; Holman, Z. C. Passivation and Carrier Selectivity of TiO<sub>2</sub> Contacts Combined with Different Passivation Layers and Electrodes for Silicon Solar Cells. In *2016 IEEE 43rd Photovoltaic Specialists Conference (PVSC)*; 2016; pp. 2403–2407.
- (27) Cho, J.; Debucquoy, M.; Recaman Payo, M.; Malik, S.; Filipič, M.; Radhakrishnan, H. S.; Bearda, T.; Gordon, I.; Szlufcik, J.; Poortmans, J. Contact Resistivity Reduction on Lowly-Doped n-Type Si Using a Low Workfunction Metal and a Thin TiO<sub>x</sub> Interfacial Layer for Doping-Free Si Solar Cells. *Energy Procedia* **2017**, *124*, 842–850.

- (28) Bullock, J.; Ota, H.; Wang, H.; Xu, Z.; Essig, S.; Samundsett, C.; Yan, D.; Hettick, M.; Morales-Masis, M.; Wan, Y.; et al. Microchannel Contacting of Crystalline Silicon Solar Cells. *Sci. Rep.* **2017**, *7*, 9085.
- (29) Bae, D.; Seger, B.; Vesborg, P. C. K.; Hansen, O.; Chorkendorff, I. Strategies for Stable Water Splitting via Protected Photoelectrodes. *Chem. Soc. Rev.* **2017**, *46*, 1933–1954.
- (30) Richards, B. S.; Richards, S. R.; Boreland, M. B.; Jamieson, D. N. High Temperature Processing of TiO<sub>2</sub> Thin Films for Application in Silicon Solar Cells. *J. Vac. Sci. Technol. Vac. Surf. Films* **2004**, *22*, 339–348.
- (31) Alén, P.; Vehkamäki, M.; Ritala, M.; Leskelä, M. Diffusion Barrier Properties of Atomic Layer Deposited Ultrathin Ta<sub>2</sub>O<sub>5</sub> and TiO<sub>2</sub> Films. *J. Electrochem. Soc.* **2006**, *153*, G304–G308.
- (32) Plagwitz, H.; Nerding, M.; Ott, N.; Strunk, H. P.; Brendel, R. Low-Temperature Formation of Local Al Contacts to a-Si:H-Passivated Si Wafers. *Prog. Photovolt. Res. Appl.* **2004**, *12*, 47–54.
- (33) Bullock, J.; Yan, D.; Wan, Y.; Cuevas, A.; Demaurex, B.; Hessler-Wyser, A.; De Wolf, S. Amorphous Silicon Passivated Contacts for Diffused Junction Silicon Solar Cells. *J. Appl. Phys.* **2014**, *115*, 163703.
- (34) Bullock, J.; Cuevas, A.; Yan, D.; Demaurex, B.; Hessler-Wyser, A.; De Wolf, S. Amorphous Silicon Enhanced Metal-Insulator-Semiconductor Contacts for Silicon Solar Cells. *J. Appl. Phys.* **2014**, *116*, 163706.
- (35) Schroder, D. K. *Semiconductor Material and Device Characterization*; 3rd edition.; John Wiley & Sons, pp. 389–465: Hoboken, New Jersey, USA, 2006.